Transparent boundary conditions for time-dependent electron transport in the R-matrix method with applications to nanostructured interfaces

G. A. Nemnes[a,b,*], Alexandra Palici[a], A. Manolescu[c]

[a] *University of Bucharest, Faculty of Physics, Materials and Devices for Electronics and Optoelectronics Research Center, 077125 Magurele-Ilfov, Romania*

[b] *Horia Hulubei National Institute for Physics and Nuclear Engineering, 077126 Magurele-Ilfov, Romania*

[c] *School of Science and Engineering, Reykjavik University, Menntavegur 1, IS-101 Reykjavik, Iceland*

Abstract

Transparent boundary conditions for the time-dependent Schrödinger equation are implemented using the R-matrix method. The employed scattering formalism is suitable for describing open quantum systems and provides the framework for the time-dependent coherent transport. Transmission and reflection of wave functions at the edges of a finite quantum system are essential for an accurate and efficient description of the time-dependent processes on large time scales. We detail the computational method and point out the numerical advantages stemming from the open system approach based on the R-matrix formalism. The approach is used here to describe time-dependent transport across nanostructured interfaces relevant for photovoltaic applications.

Keywords: transparent boundary conditions, electron transport, time-dependent Schrödinger equation, scattering formalism, nanostructured interface

*Corresponding author. Tel.: +40 (0)21 457 4949/157.
E-mail address: nemnes@solid.fizica.unibuc.ro (G.A. Nemnes).

1. Introduction

By continuing miniaturization the current electronic devices have already reached length scales of only a few tens of nanometers and, in the past few years, quantum mechanical approaches have been extensively used for the modelling of the electron transport down to molecular scale [1, 2]. In particular, there is a lot of interest for an efficient description of time-dependent coherent transport and examples of physical systems may include nanoscopic antennas [3], electron and hole transport through nanostructured interfaces with applications in photovoltaics [4], high frequency transistors [5], coherent phonon pulses in the description of transient thermal transport [6] etc.

Time-dependent charge transport has been investigated in a number of studies, using different techniques. The Green-Keldysh formalism has been applied to transport in mesoscopic systems having external time-dependent voltages [7] or barriers [8]. The Lippmann-Schwinger equation was employed in the context of wave packets propagation in quantum wires with magnetic fields [13]. More recently the time-dependent wavepacket diffusion (TDWPD) method was employed as an approximation to the exact stochastic Schrödinger equation (SSE) method [14].

In the description of the time-dependent evolution of the wavefunctions an essential ingredient is represented by the *transparent boundary conditions* (TBCs) [15]. Similar problematics is found in beam propagation in optics [16]. As the system under direct numerical investigation is finite, the TBCs are required in order to ensure the wave propagation over the boundaries. Otherwise, the waves may be partly or completely reflected back into the region of interest, bringing a limitation regarding the maximum time scales for which the process can be investigated. These are related to the size of the scattering region, which, in turn, determines the computational cost.

In this context we employ the R-matrix method as an efficient approach to obtain the stationary scattering functions. The formalism was developed by Wigner and Eisenbud [17] in the field of nuclear physics and later was employed to obtain the transport properties of mesoscopic devices [18, 19, 20]. It has been further applied to describe coherent charge transport in nanotransistors [21, 22, 23], thermopower in quantum wires [24] spin dependent transport [25] and to investigate the effects of graded distribution of scattering centers on ballistic transport [26] and charge localization in dendritic interfaces relevant for photovoltaic applications [27]. Here we use the advantages of this approach as a basis for solving the time-dependent problem

with TBCs.

Furthermore, an accurate description of many electronic devices of practical interest usually require a quantum approach at small length scales (e.g. atomistic, effective mass models) and a classical description at macroscopic scales (e.g. drift-diffusion type models), usually combined in hybrid transport models, such as the drift diffusion model (QDD) [31], the quantum corrected drift diffusion model (QCDD) [32] or the Schrödinger-Poisson-Drift-Diffusion model (SPDD) [33]. In this context of transport model hierarchies we discuss the possibility of using the developed time-dependent framework for a local characterization of the photo-current and charge separation that occurs in the vicinity of the nanostructured interfaces of photovoltaic devices.

The paper is organized as follows. In the next section the generic model system is indicated and the general R-matrix formalism is presented, pointing out the efficiency of the method in constructing the stationary scattering wavefunctions for a relatively large set of total energies. The time dependent solutions are then determined using the eigenvectors of the open quantum system. The computational method is discussed in detail. In the following section the charge transport across nanostructured interfaces relevant for photovoltaic applications is analyzed. This includes the time-dependent description of the charge separation and photo-current near the interface.

2. Model and Computational method

2.1. Coherent scattering model

The model system, depicted in Fig. 1, consists of a central finite region, Ω_0, connected by semi-infinite leads, Ω_s, which describes a multi-terminal device. This framework is typically used in the Landauer-Büttiker formalism and can also employed in atomistic transport calculations [30]. Carriers are injected from each terminal and elastically scattered in the central region Ω_0. The potential energy $V(\mathbf{r} \in \Omega_0) \equiv V_{\Omega_0}$ in central region is arbitrary, while the potentials along the lead direction in the Ω_s domains are constant, i.e. $V(\mathbf{r} \in \Omega_s) \equiv V_{\Omega_s} = V^{\perp}(\mathbf{r}_s^{\perp}) + V_s^{\parallel}$.

2.2. The R-matrix method

We consider the stationary Schrödinger equation

$$\mathcal{H}\Psi(\vec{r}) = E\Psi(\vec{r}), \tag{1}$$

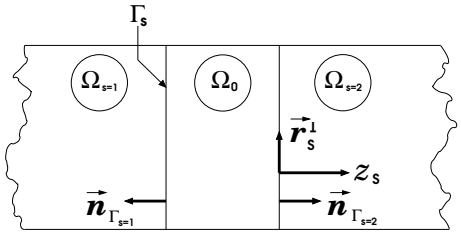

Figure 1: Two-terminal scattering model system: scattering region Ω_0 connected by leads, represented by Ω_s domains. The interfaces between Ω_0 and Ω_s are denoted by Γ_s. A reference system is indicated in each lead $(z_s, \mathbf{r}_s^\perp)$.

with $\mathcal{H} = -\hbar^2/(2m^*) \triangle + V(\mathbf{r})$, subject to scattering boundary conditions, i.e. the particles are coming from one of the leads Ω_s, commonly termed as asymptotic boundary conditions, since the electrons are coming from $z_s \to \infty$. The solutions of Eq. (1) are the scattering functions $\Psi(\vec{r})$ corresponding to the total energy E, which may vary continuously.

The wavefunctions inside the leads can be generically written as:

$$\begin{aligned} \Psi_s(\vec{r} \in \Omega_s; E) &= \sum_i \Psi_\nu^{in} \exp\left(-ik_\nu z_s\right) \Phi_\nu(\mathbf{r}_s^\perp) \\ &+ \sum_i \Psi_\nu^{out} \exp\left(ik_\nu z_s\right) \Phi_\nu(\mathbf{r}_s^\perp), \end{aligned} \tag{2}$$

where $k_\nu = \sqrt{\frac{2m^*}{\hbar^2}(E - E_\perp^\nu)}$ are the wavevectors along the transport direction in each channel ν. The composite index $\nu = (s, i)$ denotes the channel i from lead s. The complex coefficients Ψ_ν^{in} and Ψ_ν^{out} are the amplitudes of the incoming and outgoing wavefunctions for each channel, with respect to the scattering region Ω_0. The energies $E_\perp^\nu$ correspond to the transverse modes Φ_ν inside the leads, which are solutions of the transversal Schrödinger equation $(\mathbf{r}_s^\perp \in \Omega_s)$:

$$\left[-\frac{\hbar^2}{2m^*} \triangle_{\perp;s} + V(\mathbf{r} \in \Omega_s)\right] \Phi_\nu(\mathbf{r}_s^\perp) = E_\perp^\nu \Phi_\nu(\mathbf{r}_s^\perp). \tag{3}$$

To obtain the solution of the scattering problem, one solves first the auxiliary Wigner-Eisenbud (W-E) problem, which is defined on the scattering region Ω_0 as the same Schrödinger equation as in Eq. (1), with new boundary conditions on the interfaces Γ_s:

$$\mathcal{H}\chi_l(\mathbf{r} \in \Omega_0) = E_l \chi_l(\mathbf{r} \in \Omega_0), \tag{4}$$

$$\left[\frac{\partial \chi_l}{\partial z_s}\right]_{\Gamma_s} = 0. \tag{5}$$

One may further write the scattering functions in Ω_0 as linear combinations of the W-E eigenfunctions χ_l as:

$$\Psi(\mathbf{r} \in \Omega_0; E) = \sum_l a_l(E)\chi_l(\mathbf{r} \in \Omega_0). \tag{6}$$

By imposing the continuity relations on each lead - scattering region interface Γ_s, for the scattering functions and the current:

$$\Psi(\mathbf{r})|_{\Gamma_s} = \Psi_s(\mathbf{r})|_{\Gamma_s} \tag{7}$$

$$\frac{1}{m^*}\frac{\partial \Psi(\mathbf{r})}{\partial z_s}\bigg|_{\Gamma_s} = \frac{1}{m^*}\frac{\partial \Psi_s(\mathbf{r})}{\partial z_s}\bigg|_{\Gamma_s} \tag{8}$$

one obtains the relation between the incoming and outgoing coefficients Ψ_ν^{in} and Ψ_ν^{out}. In a compact form it may be written as $\vec{\Psi}^{out} = \mathrm{S}\vec{\Psi}^{in}$, where S is the scattering matrix.

The S-matrix can be conveniently expressed in terms of an R-matrix [21]:

$$\mathrm{S} = -\left[1 - \frac{i}{m^*}\mathrm{Rk}\right]^{-1}\left[1 + \frac{i}{m^*}\mathrm{Rk}\right] \tag{9}$$

where

$$\mathrm{R}_{\nu\nu'}(E) = -\frac{\hbar^2}{2}\sum_{l=0}^{\infty}\frac{(\chi_l)_\nu(\chi_l^*)_{\nu'}}{E - E_l}, \tag{10}$$

with

$$(\chi_l)_\nu = \int_{\Gamma_s} d\Gamma_s \Phi_\nu(\mathbf{r}_s^\perp)\chi_l(\mathbf{r} \in \Gamma_s). \tag{11}$$

The k-matrix is diagonal, $\mathrm{k}_{\nu\nu'} = k_\nu \delta_{\nu\nu'}$.

The scattering functions can be determined for each energy using the scattering S-matrix. Assuming the particle is incident on channel ν, i.e. from lead s and having the transversal mode i, one may write the wavefunction inside the lead s'' as:

$$\begin{aligned}\Psi_\nu(\mathbf{r} \in \Omega_{s''}; E) &= \frac{1}{\sqrt{2\pi}}\sum_{\nu'}\left[\exp\left(-ik_{\nu'}z_{s'}\right)\delta_{\nu'\nu}\right. \\ &+ \left.\mathrm{S}^t_{\nu\nu'}\exp\left(ik_{\nu'}z_{s'}\right)\right]\Phi_{\nu'}(\mathbf{r}_{s'}^\perp)\,\delta_{s's''}\end{aligned} \tag{12}$$

while in the scattering region we have:

$$\Psi_\nu(\mathbf{r} \in \Omega_0; E) = \frac{i}{\sqrt{2\pi}} \sum_{\nu'} (1 - \mathrm{S}^t)_{\nu\nu'} \mathrm{k}_{\nu'} \bar{R}_{\nu'}(\mathbf{r} \in \Omega_0; E) \tag{13}$$

with

$$\bar{R}_\nu(\mathbf{r} \in \Omega_0; E) = \int_{\Gamma_s} d\Gamma_s \, \mathcal{R}(\mathbf{r} \in \Omega_0, \mathbf{r}' \in \Gamma_s; E) \, \Phi_\nu(\mathbf{r}_s^\perp) \tag{14}$$

and

$$\mathcal{R}(\mathbf{r} \in \Omega_0, \mathbf{r}' \in \Omega_0; E) = \frac{\hbar^2}{2} \sum_l \frac{\chi_l(\mathbf{r} \in \Omega_0)\chi_l(\mathbf{r}' \in \Omega_0)}{E - E_l} \tag{15}$$

Depending on the total energy E we distinguish between open (propagating) channels with real k_ν for $E_\perp^\nu \leq E$, and closed (non-propagating) channels with imaginary k_ν for $E_\perp^\nu > E$.

The transmission functions can be determined for each pair of propagating modes and each energy E from the unitary matrix $\tilde{\mathrm{S}} = \mathrm{k}^{1/2}\mathrm{S}\mathrm{k}^{-1/2}$: $\mathcal{T}_{\nu\nu'} = |\tilde{\mathrm{S}}_{\nu\nu'}|^2$. The total lead-to-lead transmission can be calculated as: $T_{ss'} = \sum_{i,i'} \mathcal{T}_{\nu\nu'}$, where the summation is performed only over the open channels.

2.3. Time-dependent problem

Using the R-matrix method the scattering wavefunctions can be calculated for an energy E, which may vary continuously. Being solutions of the stationary Schrödinger equation (1) the functions $\Psi_\nu(\mathbf{r}; E)$ form an orthogonal system:

$$\langle \Psi_\nu(\mathbf{r}; E) | \Psi_{\nu'}(\mathbf{r}; E') \rangle = \delta_{\nu\nu'} \delta(E - E'). \tag{16}$$

In practical calculations, we discretize the energy axis and use a finite set of energies $\{E_k\}_k$.

We assume the initial quantum state of a particle is given by $\Psi(\mathbf{r}, t = 0) \equiv \Psi_0(\mathbf{r})$, typically, although not restricted to, a wavepacket inside the scattering region. For a time independent scattering potential, the time evolution is described by:

$$\Psi(\mathbf{r}, t) = \sum_{k,\nu} C_{k,\nu} \Psi_\nu(\mathbf{r}; E_k) \exp\left(-i \frac{E_k}{\hbar} t\right), \tag{17}$$

where $C_{k,\nu} = \langle \Psi_\nu(\mathbf{r}; E_k) | \Psi_0(\mathbf{r}) \rangle$ are the expansion coefficients of the initial wavefunction in the orthonormated basis made of the scattering functions.

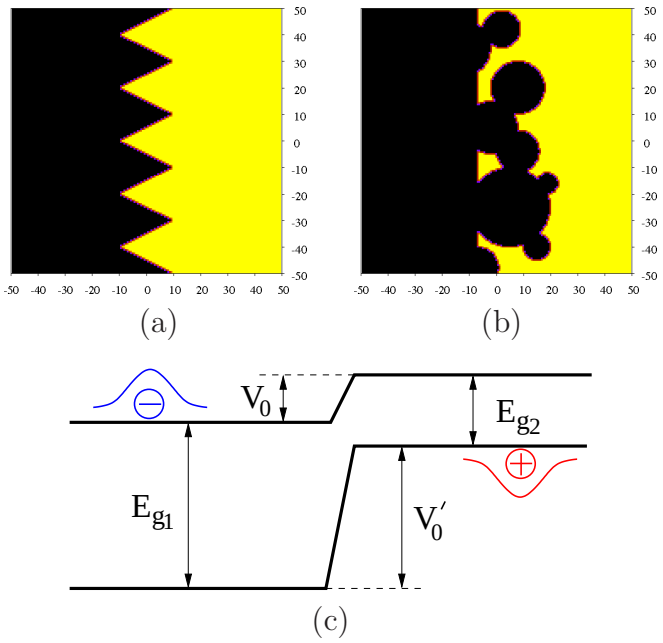

Figure 2: (a) Zig-zag and (b) mesoporous type interfaces, inside the scattering region Ω_0. The black (left hand side) regions correspond to the reference potential, while the yellow (right hand side) regions correspond to the band offsets. (c) Band offsets for electrons (V_0) and holes (V_0').

2.4. Computational method

The main advantage of the R-matrix method relies on the fact that total computational cost is divided in two parts: in the first part, the solution of the Wigner-Eisenbud problem $\{(\chi_l, E_l)\}_l$, the transversal eigenvalue problem in each lead $\{\Phi_\nu(\mathbf{r}_s^\perp), E_\perp^\nu\}_l$ and the calculation of the overlap integrals $(\chi_l)_\nu$ do not depend on the total energy E; in the second part, the R-matrix, the S-matrix and optionally transmission functions and scattering wavefunctions are determined for each total energy E. Usually, for moderate number of channels and a large enough basis set, the Hamiltonian diagonalization performed in order to obtain the eigensystem $\{(\chi_l, E_l)\}_l$ represents the largest computational cost. This step is performed only once, while the energy dependent calculations require a much smaller computational effort. The advantage of this method becomes particularly important when a relatively large number of transmissions and wavefunctions need to be determined. In the following we detail the computational steps in our approach.

The rank of the Hamiltonian matrix in a three-dimensional model ($d =$

3) is $N_b = N_{bx} \times N_{by} \times N_{bz}$, where N_{bx}, N_{by}, N_{bz} are the numbers of basis functions corresponding to each spatial dimension. The basis functions $\phi_{ijk}(\mathbf{r}) = \phi_{xi}(x) \times \phi_{yj}(y) \times \phi_{zk}(z)$ defined in Ω_0 should obey the vanishing normal derivative imposed by the condition (5) at the planar interfaces with the leads Ω_s. Although specific geometries require different basis sets, a generic model consists of identifying Ω_0 with a parallelipipedic box of volume $L_x \times L_y \times L_z$. Assuming the origin of the coordinate system is in the middle of Ω_0, we may choose $\phi_{xi}(x) = 1/\sqrt{L_x}\cos(i\pi(x+L_x/2)/L_x)$, with $i = 1, 2, \ldots$ and similarly for $\phi_{yj}(y)$ and $\phi_{zk}(z)$. By a one-time diagonalization, of typical cost $\mathcal{O}(N_b^3)$, the Wigner-Eisenbud functions and energies are determined. The transversal modes $\Phi_\nu(\mathbf{r}_s^\perp)$ are found by solving Eq. (3) in each lead Ω_s, which are $(d-1)$-dimensional problems and therefore require a significantly lower computational cost, compared to the Wigner-Eisenbud problem.

In the following one needs to set the maximum number of channels n_s considered in each lead, the total number of channels $N_{\rm ch} = \sum_s n_s$ being the rank of the R- and S-matrices, which are rigorously infinite matrices. The number of channels n_s should be large enough to include at least the open channels and an appropriate number of closed ones, to ensure the convergence of the calculations, in particular of the transmission functions. At this point one can calculate explicitly the integrals $(\chi_l)_\nu$ from Eq. (11). One should note that all these steps are energy independent.

In the second step, the R-matrix elements for a particular total energy E are found by simple summations, of total cost $\mathcal{O}(N_b \times N_{\rm ch}^2)$. As the k-matrix is diagonal, finding the matrices $[1 \pm \frac{i}{m^*}\mathrm{Rk}]$ from Eq. (9) is achieved by an insignificant cost of $\mathcal{O}(N_{\rm ch})$. The most demanding part is the computation of the inverse of the dense matrix $[1 - \frac{i}{m^*}\mathrm{Rk}]$, which may be performed by standard LAPACK [34] routines with scaling of $\mathcal{O}(N_{\rm ch}^3)$. The subsequent matrix multiplication in Eq. (9) and the similarity transform used to obtain the $\tilde{\mathrm{S}}$ matrix do not exceed the computational cost of matrix inversion. These steps are performed for a number of N_E total energies, so that the total cost is $\mathcal{O}(N_E \times N_{\rm ch}^3)$. If $N_{\rm ch} \ll N_b$, which is a typical situation, the computational burden mostly falls on solving the Wigner-Eisenbud problem. One should note that for an accurate representation of the $\Phi_\nu(\mathbf{r}_s^\perp)$ transversal modes, the number of channels considered in the calculations should be significantly smaller than the number of basis elements used for diagonalizing the leads Hamiltonian given by Eq. (3). The total cost of finding the transmission functions is $\mathcal{O}(N_b^3 + N_E \times N_{\rm ch}^3)$ and one can easily see that the cost of energy dependent part becomes comparable to the Wigner-Eisenbud problem only if

the transmissions are computed for a large number of total energies, making the procedure effective in providing rapid varying transmission functions.

One should point out that the R-matrix method provides the set of scattering functions $\{\Psi_\nu(\mathbf{r}; E_k)\}_{\nu,k}$ of the open quantum system, which are continuous over the entire interval, leads and scattering region. One advantage of our method is the possibility of including potential barriers at the lead/scattering region interfaces, of arbitrary height, and therefore to tune the contacts to the leads from fully transparent for electrons (or reflectionless) with no barrier, to almost opaque with high barriers. An even bigger advantage is the fully transparent case itself, which practically describes an infinite system with a finite Hamiltonian matrix in the scattering region and asymptotic wave functions outside. Alternatively, a large system can in principle be described as a finite, closed system, in a basis of wave functions vanishing at the boundaries. But for practical calculations the size of the basis must increase with the size of the system, eventually becoming prohibitive. Therefore, for given physical parameters and simulation time our method is more efficient. While the solution of the Wigner-Eisenbud problem represents usually the most demanding part, the presence of the leads generates only a minimal additional computational effort.

3. Application to nanostructured interfaces

3.1. Physical systems

Nanostructured inhomogeneous interfaces increase the light scattering and the device active area in photovoltaic applications, enhancing the generation of photoexcited carriers. The size of the inhomogeneities should be comparable with the light wavelength, i.e. hundreds of nanometers. Different techniques have been used to achieve this goal, e.g. by using nanowire arrays or mesoporous materials. The latter have been increasingly used for boosting the solar cell efficiencies. As concrete examples, one can mention thin films of nearly spherical TiO_2 or ZnO aggregates with typical sizes up to a micron. Furthermore, the aggregates possess inner structure, being composed of nanocrystallites, with typical sizes of $\sim$15nm [38]. Given the quite different length scales involved in the physical structures of interest and the operation conditions, hybrid (quantum-classical) transport models should be used: at a few nanometer length scales, e.g. at the nanocrystallite scale, a quantum mechanical transport model should be best suited, while at the aggregate level and larger scales a drift-diffusion model should be employed.

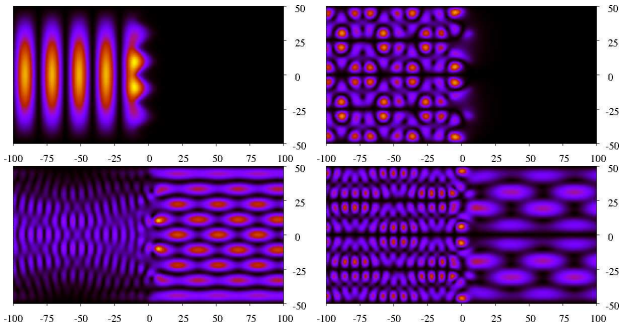

Figure 3: Zig-zag interface: scattering wavefunctions (absolute value square) for (a) lowest transverval mode for total energies $E = 0.015$ eV (upper), 0.15 eV (lower) and (b) the 8th mode for $E = 0.09, 0.15$ eV. The bandoffset potential is $V_0 = 0.1$ eV. The images include the scattering region and portions of the leads as described in the text. The scattering region corresponds to the interval $(-50, 50)$ nm on the horizontal direction.

We consider here two different types of nanostructured interfaces, namely the *zig-zag* and the *mesoporous* interface, as indicated in Fig. 2. The first interface presents sharp regular variations, while the second one mimics a prototypical mesoporous layer. Flat-band condition is assumed for each of the two materials in the bulk, while at the interface there is a band offset V_0. Both types of structures introduce a local confinement potential for electrons and holes. From the holes perspective, the potentials in Fig. 2 are simply interchanged, provided the bandgap is the same in the two materials. Generally, for different bandgaps in the two materials, E_{g1} and E_{g2}, the band offset for holes is $V_0' = E_{g1} - E_{g2} + V_0$. Therefore, in a non-interacting one-particle picture, we may describe within the same formalism the independent propagation of electrons and holes across the nanostructured interface [27].

3.2. Scattering wavefunctions

We first analyze the solution of the stationary Schrödinger equation (1), subject to scattering boundary conditions for the two types of interfaces.

Typical scattering wavefunctions for electrons are depicted in Figs. 3 and 4 for the zig-zag and the mesoporous interface, for two different transversal modes, 1st and 8th, and different total energies and band offsets. The wavefunctions are shown for the combined system of leads (Ω_s) and scattering region (Ω_0). We consider a rectangular scattering region defined by the lengths $L_x = L_y = 100$ nm as shown in Fig. 2 and additional portions of

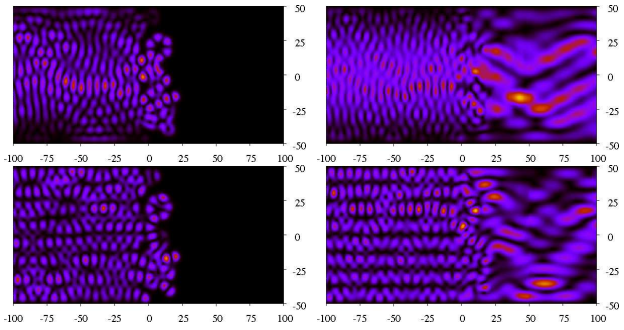

Figure 4: Mesoporous interface: scattering wavefunctions (absolute value square) for (a) 1st and 8th modes with $E = 0.18$ eV (upper) and $V_0 = 0.5$ eV (lower); (b) the same modes and total energy, but for a lower bandoffset, $V_0 = 0.1$ eV.

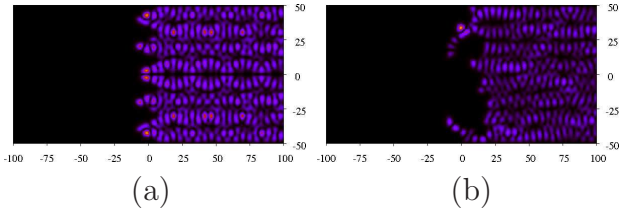

Figure 5: Scattering functions (absolute value square) corresponding to holes incoming from right, for the zig-zag (a) and mesoporous (b) interfaces. The 8th mode is represented at $E = 0.3$ eV, for a band offset $V_0' = 0.5$ eV.

the leads of length $L_s = 50$ nm are also depicted. At energies lower than the band offsets, there is total reflection, since the V_0 potential step extends in the right lead to infinity. At higher energies, transmitted wavefunctions are observed in the right lead, together with partial reflections into the left lead. As one can see from Fig. 3 the regular shaped zig-zag interface produces uniform patterns in the scattering functions and therefore in the charge localization. On the other hand, in the case of a disordered mesoporous interface, as one may expect, asymmetries due to randomness are present. The shapes of the scattering potential can be correlated to the maxima of localization, which indicates the feasibility of our approach in the context of describing fine-grain nanostructured interfaces. We also refer the reader to Ref. [27] where sharp dendritic interfaces were analyzed.

In the effective mass model, the hole perspective is mirrored with respect to the electron picture. Figure 5 shows the scattering wavefunctions for holes,

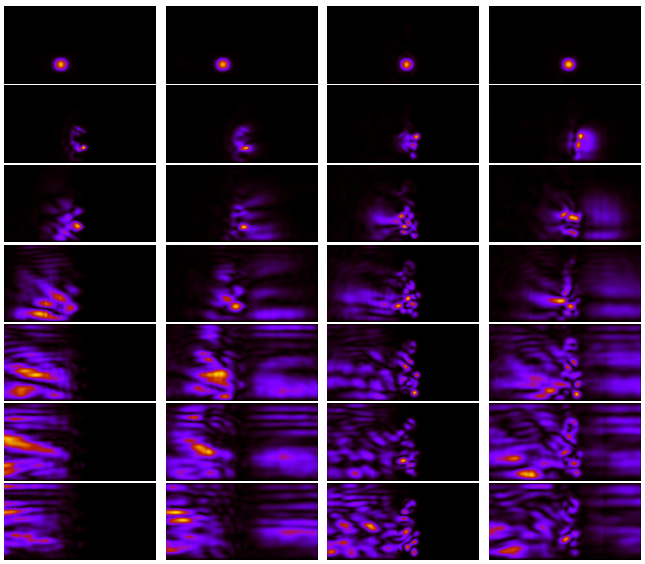

Figure 6: Snapshots of the wavepacket scattering for the zig-zag interface (a,b) and for the mesoporous interface (c,d), starting with $t_0 = 0$ in steps of 0.04 ps from top to bottom. For (a,c) the bandoffset is $V_0 = 0.3$ eV, leading to a complete reflection of the wavepacket, while for (b,d) $V_0 = 0.1$ eV and partly transmitted electron waves are visible. For a better visibility, the colormap has been rescaled in each plot.

which are incoming from the right hand side. For the chosen parameters, $E = 0.3$ eV and $V_0' = 0.5$ eV, the holes are completely reflected and the two localization probability maps become complementary to the ones obtained for electrons: for the zig-zag interface, see Fig. 3(b) (upper part) and for the mesoporous interface, see Fig. 4(a) (lower part).

3.3. Wavepacket propagation

We assume wavepackets are generated near the nanostructured interface, corresponding to either electrons or holes. The initial wavepacket is described by a plane wave modulated by a Gaussian function

$$\Psi_0(\mathbf{r}) = A \cdot \Theta(\mathbf{r}; \mathbf{r}_0, R_c) \cdot \exp\left[-\frac{|\mathbf{r} - \mathbf{r}_0|^2}{2\sigma^2}\right] \cdot \exp(-i\mathbf{k}_0\mathbf{r}), \tag{18}$$

where the function $\Theta(\mathbf{r}; \mathbf{r}_0, R_c)$ is 1 for $|\mathbf{r} - \mathbf{r}_0| \leq R_c$ and 0 for $|\mathbf{r} - \mathbf{r}_0| > R_c$, imposing strictly the vanishing condition for $\Psi_0(\mathbf{r})$ beyond a cutting radius R_c and A is a normalization constant. By using the Θ function one can

avoid introducing extra energy in the wavepacket as it may partly overlap with high potential energy regions.

We consider the wavepacket is incident from the left, initially located at $\mathbf{r}_0 = (x_0, y_0)$, where $x_0 = -25$ nm, $y_0 = -25$ nm for the zig-zag interface and $x_0 = 5$ nm, $y_0 = -25$ nm for the mesoporous interface, i.e. it is placed in the middle of the largest circular nanoparticle. The wavevector $\mathbf{k}_0 \equiv (10\pi/L_x, 0)$ was chosen along the x direction, while $\sigma = L_x/16$ and the effective mass is $m^* = 0.0655 m_0$ (GaAs). The cutting radius is $R_c = 10$ nm. With these parameters the kinetic energy of the particle is $E_0 = 0.14$ eV. A uniform grid with of 400 total energies E_k in the range $[0, 0.3]$ eV was considered.

Snapshots of wavepacket evolution are presented in Fig. 6, for the zig-zag interface (a,b) and the mesoporous interface (c,d). Two band offsets are considered, $V_0 = 0.1$ eV and $V_0 = 0.3$ eV, rendering a partially transparent interface and a practically opaque one, respectively. The shapes of the interfaces introduce different consequences in the wavepacket scattering. For example, the zig-zag interface tends to scatter significantly the wavepacket in the transversal direction, decreasing the kinetic energy on the x direction such that the propagation along the leads is slow. By contrast, in the case of the mesoporous interface, the largest nanoparticle is the primary scatterer and the scattered wave is more uniform. In this case the partially transmitted and reflected waves are moving away from the interface at a higher speed compared to the zig-zag interface, but some probability remains confined for a longer time at the mesoporous interface.

Although the system considered here is two-dimensional, the method can be extended to the more computationally demanding three-dimensional case. The qualitative picture regarding charge localization and transport is however qualitatively very similar, as it was pointed out in Refs. [24, 27].

3.4. Charge propagation near the nanostructured interface

Based on our time-dependent approach with transparent boundary conditions we can calculate the evolution of the charge distribution and the photo-current. Wavepackets, which correspond to the electron/hole pairs generated at the interface, are scattered elastically during a time interval which is a typical average coherence time τ_c. Our aim here is not to fully describe the current collected at the contacts as it may depend on other parameters, like e.g. recombination rates, but to describe the electron-hole separation at the nanostructured interface. Beyond τ_c the carriers may suffer

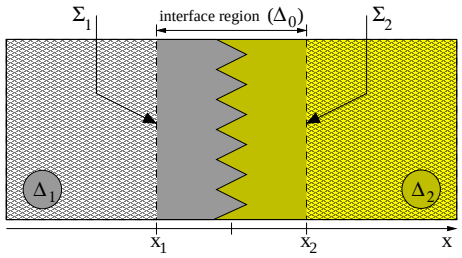

Figure 7: Schematics of the photo-current model: the interface region Δ_0 and the outer regions Δ_1 and Δ_2. Wavepackets are generated in Δ_0 and the charge separation is evaluated for each region at a typical coherence time τ_c.

inelastic scattering processes and, at even larger time scales, they diffuse towards the contacts moving through the bulk of the two materials, a process which may be further described by a classical drift-diffusion model.

In order to quantify the charge separation, we isolate the interface region Δ_0 between positions x_1 and x_2. The outer regions Δ_1 and Δ_2, correspond to the two materials which make up the junction, as depicted in Fig. 7. These three domains may possibly correspond to the Ω_0, Ω_s regions which previously defined the scattering problem. We calculate the probability of finding the particle in the Δ_s domains, Q_s, using the continuity relation for the probability current

$$Q_s(\tau_c) = \int_0^{\tau_c} dt \int_{\Sigma_s} \mathbf{j}(\mathbf{r},t)\, d\mathbf{\Sigma}_s = \int_{\Delta_s} d\mathbf{r}\, |\Psi(\mathbf{r}, t=\tau_c)|^2, \tag{19}$$

where $\mathbf{j}(\mathbf{r},t) = 1/m\mathrm{Re}[\Psi^*(\mathbf{r},t)(-i\hbar\nabla)\Psi(\mathbf{r},t)]$ is the probability current. The probabilities Q_s correspond to the amounts of charge separated by the interface, which are found in Δ_s domains at τ_c. Furthermore, one may define the current flowing into each Δ_s region as $I_s = dQ_s/dt$.

The time evolution of the charge separation is plotted in Fig. 8 for the zig-zag and mesoporous interfaces for the cases shown in Fig. 6(b) and 6(d), in comparison with an ideally flat interface positioned at $x = 0$. We define the regions Δ_s by choosing x_1 and x_2 according to Fig. 7 : $x_1 = -40$ nm, $x_2 = 10$ nm for the flat and zig-zag interfaces and $x_1 = -10$ nm, $x_2 = 40$ nm for the mesoporous interface. The interface regions have a length of 50 nm along the x direction for all three structures and include the wave packet, which has the initial coordinates $(-25, -25)$ nm in the case of the flat and zig-zag interface and $(5, -25)$ nm in the case of the mesoporous interface.

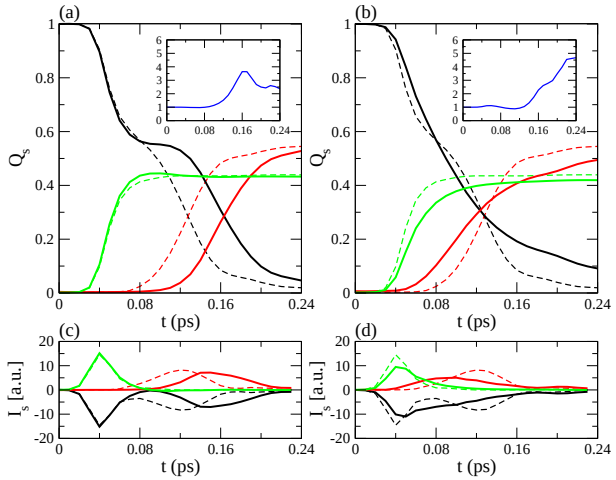

Figure 8: Integrated probability flux Q_s for the zig-zag (a) and mesoporous (b) interfaces. Q_s is calculated for the regions $\Delta 0$ (black), $\Delta 1$ (red), $\Delta 2$ (green). The dashed lines correspond to a flat interface. The insets show the ratio between Q_0 of zigzag/mesoporous interface and the same quantity corresponding to the flat interface, as an indicator of trapped charge in the Δ_0 region. The photo-currents for each region Δ_s are indicated in (c) and (d).

The wave packet is therefore in both cases initially placed mid-way between Σ_1 and Σ_2.

In the following we discuss comparatively the particularities introduced by each type of interface. The chosen band offset of $V_0 = 0.1$ eV allows partly transmitted waves. For both nanostructured interfaces we obtain, in some respect, a similar behavior for the Q_s time dependency. In the interface region Q_0 decreases, while Q_1 and Q_2 increase in time and tend to saturate. The increase of Q_1 is delayed compared with Q_2 as the wave packet moves from left to right and gets scattered at the interface. By comparison, keeping the same parameters, the zig-zag interface introduces larger delays compared with the flat one. This interface transfers part of the kinetic energy, initially on the x direction, onto the y direction, leading to a slower advance speed. In contrast, the scattering across the mesoporous interface overall resembles better the data obtained for the flat interface, with one difference: Q_0 decays slightly slower. The wave is trapped at the interface for longer times, as one can also see from the insets of Fig. 8 and also from sequence in Figs. 6(c) and (d), compared with the zig-zag interface. In addition, the increase of Q_1 and Q_2 is smoother compared to both flat and zig-zag interfaces. The lower plots show

the photo-currents in each region Δ_s: the transmitted and reflected waves are visible as current pulses of different widths. The back scattered waves arrive at the Δ_1 region at later times compared to the transmitted waves and the width of the current pulse is accordingly more dispersed. Although the time-dependent quantities $Q_s(t)$ and $I_s(t)$ depend on the specific choice of the Δ_s domains, the observed behavior remains qualitatively the same.

For a complete characterization of a certain interface one has to perform statistical averages, taking into account the variation of the wavepacket parameters ($\mathbf{k}_0$, $\mathbf{r}_0$, σ, shape etc). Moreover, averages on different interfaces from the same class would be generally necessary. To investigate the charge localization on either side of the interface, a distribution of τ_c may also be considered and subsequently a drift-diffusion type model may be employed to calculate the collected photo-current in a concrete device. Here we presented the methodology for evaluating the charge separation leaving a more complex analysis for a future study.

4. Conclusions

We introduced a general framework for describing time-dependent coherent transport using the R-matrix formalism. Expanding the time-dependent wavefunctions in the basis of scattering functions obtained by solving the stationary problem for the open quantum system, the transparent boundary conditions are introduced in a natural way. The R-matrix method provides an efficient procedure of calculation the wavefunctions for a relatively large energy set, which is essential for an accurate description of the time-dependent transport. The detailed steps of the computational scheme are provided. As applications, we consider the scattering of wavepackets across nanostructured interfaces, which become increasingly relevant for new generation of nanostructured photovoltaic devices. We discuss the transient behaviors of electrons crossing different types of interfaces. Finally, we introduce a model for calculation of the photo-current and charge localization, which provides a tool for optimizing nanostructured interfaces.

Acknowledgment

The research leading to these results has received funding from EEA Financial Mechanism 2009 - 2014 under the project contract no 8SEE/30.06.2014

and by the National Authority for Scientific Research and Innovation (ANCSI) under grant PN16420202.

References

References

[1] N. J. Tao, Nature Nanotechnology 1 (2006) 173.

[2] B. Popescu, P. B. Woiczikowski, M. Elstner, U. Kleinekathöfer, Phys. Rev. Lett. 109 (2012) 176802.

[3] S. D. Gennaro, Y. Sonnefraud, N. Verellen, P. Van Dorpe, V. V. Moshchalkov, S. A. Maier, R. F. Oulton, Nature Comm. 5 (2014) 3748.

[4] M. A. Loi and Jan C. Hummelen, Nature Mater. 12 (2013) 1087.

[5] E. Pallecchi, Q. Wilmart, A. C. Betz, S.-H. Jhang, G. Feve, J.-M. Berroir, S. Lepillet, G. Dambrine, H. Happy, B. Placais, J. Phys. D: Appl. Phys. 47 (2014) 094004.

[6] Xiang Chen, A. Chernatynskiy, Liming Xiong, Youping Chen, Comput. Phys. Commun. 195 (2015) 112.

[7] A. P. Jauho, N. S. Wingreen and Y. Meir, Phys. Rev. B 50 (1994) 5528.

[8] V. Moldoveanu, V. Gudmundsson and A. Manolescu, Phys. Rev. B 76 (2007) 165308.

[9] V. Moldoveanu, V. Gudmundsson and A. Manolescu, Phys. Rev. B 76 (2007) 085330.

[10] V. Moldoveanu, A. Manolescu, C. S. Tang, V. Gudmundsson, Phys. Rev. B 81 (2010) 155442.

[11] V. Gudmundsson, O. Jonasson, T. Arnold, Chi-Shung Tang, Hsi-Sheng Goan and A. Manolescu, Fortschritte der Physik 61 (2013) 305.

[12] N. R. Abdullah, Chi-Shung Tang, A. Manolescu and V. Gudmundsson, J. Phys.: Condens. Matter. 27 (2015) 015301.

[13] G. Thorgilsson, Chi-Shung Tang and V. Gudmundsson, Phys. Rev. B 76 (2007) 195314.

[14] Xinxin Zhong, Yi Zhao and Jianshu Cao, New J. Phys. 16 (2014) 045009.

[15] X. Antoine, A. Arnold, C. Besse, M. Ehrhardt and Achim Schädle, Commun. Comput. Phys. 4 (2008) 729.

[16] G. R. Hadley, Opt. Lett. 16 (1991) 624.

[17] E.P. Wigner, L. Eisenbud, Phys. Rev. 72 (1947) 29.

[18] L. Smrcka, Superlattices Microstruct. 8 (1990) 221.

[19] U. Wulf, J. Kucera, P.N. Racec, E. Sigmund, Phys. Rev. B 58 (1998) 16209.

[20] E. Onac, J. Kucera, U. Wulf, Phys. Rev. B 63 (2001) 085319.

[21] G. A. Nemnes, U. Wulf and P. N. Racec, J. Appl. Phys. 96 (2004) 596.

[22] G. A. Nemnes, U. Wulf and P. N. Racec, J. Appl. Phys. 98 (2005) 084308.

[23] G. A. Nemnes, L. Ion and S. Antohe, J. Appl. Phys. 106 (2009) 113714.

[24] G. A. Nemnes, L. Ion and S. Antohe, Physica E 42 (2010) 1613.

[25] G. A. Nemnes, A. Manolescu, V. Gudmundsson, J. Phys.: Conf. Series 338 (2012) 012012.

[26] T. L. Mitran, G. A. Nemnes, L. Ion and Daniela Dragoman, J. Appl. Phys. 116 (2014) 124316.

[27] G. A. Nemnes and Sorina Iftimie, Appl. Surf. Sci. 352 (2015) 158.

[28] A. Manolescu, G. A. Nemnes, A. Sitek, T. O. Rosdahl, S. I. Erlingsson and V. Gudmundsson, Phys. Rev. B 93 (2016) 205445.

[29] S. Heedt, A. Manolescu, G. A. Nemnes, W. Prost, J. Schubert, D. Grutzmacher and T. Schaepers, Nano Lett. 10.1021/acs.nanolett.6b01840 (2016).

[30] R. A. Bell, S. M.-M. Dubois, M. C. Payne, A. A. Mostofi, Comput. Phys. Commun. 193 (2015) 78.

[31] P. Degond, S. Gallego, F. Mehats, J. Comp. Phys. 221 (2007) 226.

[32] C. de Falco, J. W. Jerome, R. Sacco, J. Comp. Phys. 228 (2009) 1770.

[33] A. Pirovano, A.L. Lacaita, and A.S. Spinelli, IEEE Trans. Electron Devices 1 (2002) 25.

[34] E. Anderson, Z. Bai, C. Bischof, S. Blackford, J. Demmel, J. Dongarra, J. Du Croz, A. Greenbaum, S. Hammarling, A. McKenney, D. Sorensen, LAPACK Users Guide, third ed., Society for Industrial and Applied Mathematics, Philadelphia, PA, ISBN: 0-89871-447-8, 1999.

[35] B. A. Lippmann and J. Schwinger, Phys. Rev. 79 (1950) 469.

[36] C. S. Lent and D. J. Kirkner, J. Appl. Phys. 67 (1990) 6353.

[37] L. P. Kadanoff and G. Baym, Quantum Statistical Mechanics: Green's Function Methods in Equilibrium and Nonequilibrium Problems, Addison-Wesley (1989).

[38] Qifeng Zhang, Kwangsuk Park and Guozhong Cao, Materials Matters 5 (2010) 32.